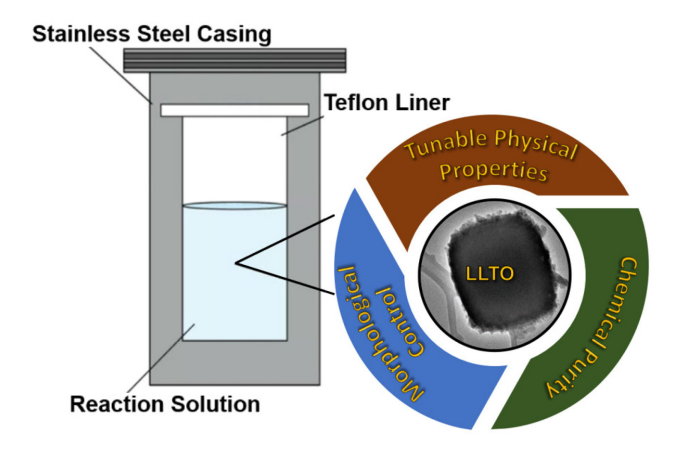
One-Step Solvothermal Synthesis of Perovskite-Type Li_{3x}La_{2/3-x} \square _{1/3-2x}TiO₃ Nanomaterials

Michael A. Dato, Linhua Hu, Dan McElheny, and Jordi Cabana*

Department of Chemistry, University of Illinois Chicago, Chicago, IL 60607, USA

E-mail: jcabana@uic.edu

Table of Contents



Abstract

Due to its high ionic and low electronic conductivity, the cubic perovskite polymorph of Li_{3x}La_{2/3-x} $\square_{1/3-2x}$ TiO₃ (c-LLTO) is considered a canonical solid electrolyte for battery applications. However, traditional solid-state synthetic protocols for this high-performing polymorph are multistep, and require high temperature sintering at temperatures over 1000°C, which creates challenges of processing and precludes the synthesis of nanomaterials that could be integrated into multifunctional, multicomponent architectures. In this study, the synthesis of c-LLTO is reported through a one-step solvothermal method in the presence of a surfactant. With this solution method, not only is it possible to obtain nanocrystals, but also to stabilize c-LLTO at much lower temperatures than in conventional solid-state syntheses. In addition, the modulation of solvent and surfactant identities alter the reaction times necessary to facilitate crystallization at multiple scales of domain size, which suggests that confinement does not play much of a role in the stabilization of the cubic phase. The changes in particle size and shape were found to impart large differences in the

measured Li dynamics through NMR, effectively illustrating that by employing a solvothermal synthetic method enables the tuning of chemical properties for a targeted application.

Introduction

Metal oxides, and more specifically perovskite-type materials, are the cornerstone of several applications, including ionic devices, $^{1.4}$ catalysis, $^{5.7}$ and lasing mediums. One such material, $\text{Li}_{3x}\text{La}_{2/3-x} \square_{1/3-2x}\text{TiO}_3$ (LLTO), has been examined for use in solid electrolytes due to its high lithium-ion conductivity and mechanical hardness, $^{9, 10}$ which is competitive with other families of materials such as garnets and LiSICON-type structures. Perovskite LLTO presents significant polymorphism, as shown in **Figure 1**, based on distortions of the B-centered (TiO₆)²⁻ octahedra, which are accompanied by Li^+ , La^{3+} , or vacancies in the A-sites, coordinated by 12 oxygen anions per site. The compositional space of LLTO reported in the literature involves x values of 0 < x < 0.16, and always has Ti^{4+} due to overall charge neutrality, thus rendering it electronically insulating. This compositional variation also affects the exact polymorph that forms (**Figure 1**).

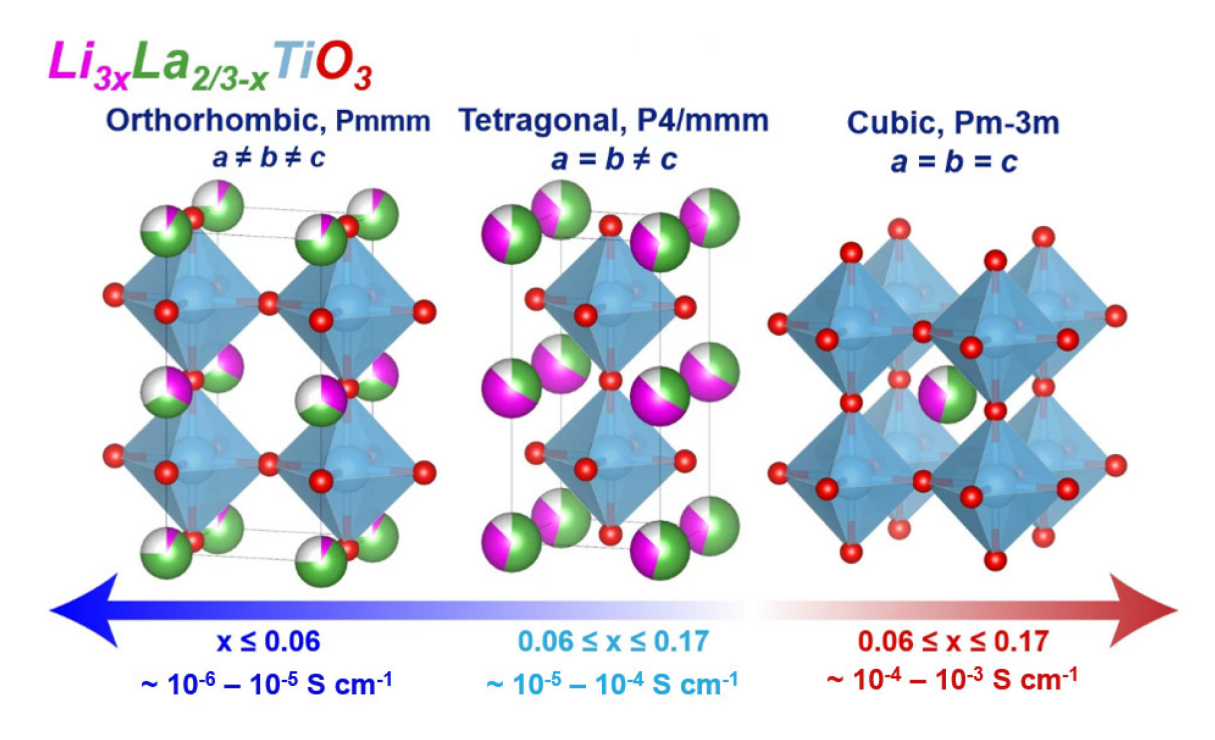


Figure 1. Representation of the three most prevalent crystal structures in the literature of LLTO, along with their representative ionic conductivities.

The cubic phase (Pm-3m space group) shows the highest Li+ conductivity, underpinned by the absence of specific ordering of ions or vacancies in the A sites. It is generally accepted that increasing vacancies or lithium concentration in the host structure will induce sufficient disorder in the A sites to yield the cubic or pseudocubic phase. ¹⁴⁻¹⁷ Distortions based on the simple cubic to other superlattices depend strongly on the Li+/La³⁺/vacancy ratios and their relative ordering, which changes the nature of the Ti-O bonds and the relative positioning of their octahedra forming the backbone of the structure. For the purposes of this report, crystallographic orientations discussed are based on the Pm-3m parent group, while others have been reported, and are commented on below. A-site cations and vacancies order along the c-axis whereby La³⁺ ions distribute unevenly in 1a (0,0,0) and 1b (0,0,1/2) sites to produce the tetragonal lattice (P4/mmm) with parameters $a = b = a_p$ and $c \approx 2a_p$ (where a_p represents the equivalent cubic cell parameter), shown in the middle of **Figure 1** as a double perovskite. ¹⁸⁻²⁰ In XRD this results in superstructural peak splitting for reflections with l = 2n + 1. ^{18,19} Orthorhombic (Pmmm) distortions based on tetragonal ordering result from an arrangement of ions along the c-axis at low lithium concentrations (x > 0.06 in Li_{3x}La_{2/3-x} \square _{1/3-2x}TiO₃). This presents crystal parameters such that $a \ne b \ne c$ and is accompanied by the slight tilting of the octahedra

to accommodate changes in local electric field gradients (**Figure 1**). This generally leads to specific diffraction splitting to three peaks for every XRD line besides the (111) direction, resulting from three unique crystallographic directions.²¹

Dopant concentrations and their relative ordering is largely driven by reaction temperature and heat treatment.^{22, 23} Conventional solid-state or modified solution-gelation protocols call for high-temperature sintering (500-1400°C) in order to yield a single phase material, and often require intermittent grinding steps to produce homogenous samples. 15, 24-28 The target phase of this report, Pm-3m, has been generally stabilized following sintering temperatures near or above 1200 °C.^{29, 30} Traditionally, cubic perovskites are not accessible without some special temperature treatment that impacts the relaxation process upon cooling, including flash sintering or quenching. 17, 31, 32 Additionally, the substitution with some stabilizing fourth metal has shown to aid in cubic stabilization. ^{20, 33, 34} The literature suggests these methods prevent phase transitions upon cooling to ambient by Li ordering or loss through volatilization sustained at high temperatures. ^{15, 18, 35, 36} Control of dopant ratios at such high temperatures preclude many sintering methods from being a reliable method of targeting metastable oxides. At lower synthesis temperatures and without heat treatment, the effective ordering of the dopants yields more thermally stabilized polymorphs. Tetragonal double perovskites have been synthesized in the range of about 700 - 1300 °C. ^{21, 37-39} Orthorhombic phases have been reported at sintering temperatures near or above 600 °C.^{21, 37} As informed by the discussion of crystallographic substitutions, there is a general trend that cationic order correlates negatively with sintering temperature, and that naturally, the most ordered titanates are more accessible at lower temperatures.

Generally, observed differences in ionic conductivities in LLTO samples can be attributed to both crystal phase and sample morphology, which are outcomes of the chosen synthetic method. The effective ionic conductivity of any electrolyte material generally depends upon charge carrier concentration and the degree of ionic motion. For the mobility of Li⁺ through the host, symmetry constraints placed on the A-site result in bottlenecks that limit the ability of lithium to exchange places with an adjacent vacancy. Additionally

important is the morphology, as polycrystalline secondary structures present additional barriers to ionic motion through grain boundaries, arising from the incomplete contact of primary particles, and are most prevalent in solid-solid or sol-gel protocols. 15, 24-28 The highest ionic conductivity measured for the undoped cubic polymorph is on the order of 10⁻³ S cm⁻¹ at room temperature, first reported by Belous et al. in 1987, then later by Inaguma et al. in 1993.^{40, 41} This is generally observed for samples where $x \approx 0.1$, meaning that charge carrier concentration is optimized alongside Li⁺ mobility near this concentration. Distorted structures generally show precipitous losses in ionic conductivity, namely for tetragonal (10⁻⁵ – 10⁻⁴ S cm⁻ 1) and orthorhombic (10⁻⁶ – 10⁻⁵ S cm⁻¹) lattices, which are attributed to lower lithium concentrations and structural bottlenecks. 18, 23-27 High quality nanoparticles would open up pathways for fabrication of highly tailored multifunctional architectures such as inorganic-polymer hybrid electrolytes. 42-45 For this, the dispersion of particulate matter in a host solvent before their incorporation into a polymer matrix, and therefore engineering smaller particles would be useful for processability (Figure S2). Grain boundary resistances, which result from a large impedance between the charged surfaces of primary particles, severely limit applicable charge rates by bottlenecking ionic conductivity by several orders of magnitude relative to the bulk, particularly for LLTO. 25, 26, 35, 39, 43 Measurements of small particulates pressed into an electrolyte have shown large rises in impedance which severely limit performance.^{25, 46, 47} However, the processability of nanoparticles may render them advantageous in the fabrication of high-quality green bodies that are turned into very dense microcrystalline pellets upon applying conventional sintering techniques.⁴⁸

Efforts in turning away from high-temperature sintering protocols have led to the implementation of solution-based syntheses for challenging metal oxide products, particularly in the form of nanocrystals. Solvothermal synthesis has a prominent role when targeting metastable metal oxides more broadly, ^{49, 50} as well as challenging perovskites. ⁵¹⁻⁵⁴ Often, the goal of a typical solvothermal synthesis for a metal oxide is to place a somewhat volatile backbone precursor in an environment that promotes hydrolysis and polymerization in polar media, much like that of a gelation reaction, which may be stabilized by the

intercalation of cations into the anionic host.^{55, 56} Several papers have shown the formation of LLTO solvothermally; however, either the thermodynamically favored tetragonal polymorph is made, or the control over particle morphology was not explored.⁵⁷⁻⁵⁹ These methods could also be further expanded by including a surfactant during synthesis, which pushes the solution past its triple point during temperature ramping and results in a severe reduction in system dielectric and therefore solubility,^{60, 61} facilitating the crystallization of a capped crystalline material. It is well established that, in these cases, the identities of all chemical substituents and oven protocols will have influence on the chemistry, size, and shape of the materials targeted.^{52-54, 62} This strategy has not been explored in the case of c-LLTO.

In this account, nanocrystals of the cubic polymorph of LLTO (c-LLTO, hereafter) successfully synthesized via solvothermal protocols. These nanocrystals were shown to form stable dispersions in ethanol for over one week. To probe more closely the influences of reaction environment on phase stability, solvent and surfactant identities were altered. Overall, the unique stability of c-LLTO via solution-based processing is established, where size and shape of the material may be tailored toward specific applications, namely for hybrid solid electrolytes.

Materials and Methods

Ethanol (200 proof); ethylene glycol (99%); lithium acetate (99%); lanthanum (III) nitrate hexahydrate (99.999%); oleic acid (90%); sodium hydroxide (97%); titanium (IV) butoxide (97%) were purchased from Sigma-Aldrich and used as received.

The synthetic method was adapted from a previous study.^{53, 54} In a typical synthesis, 0.75 mmol of lithium and lanthanum precursors were dissolved in 15 mL of deionized water, making Solution 1. Then, 1.2 g of sodium hydroxide was dissolved in 6 mL of DI water, making Solution 2. To make Solution 3, 1.5 mmol of titanium (IV) butoxide was dissolved in absolute ethanol contained within an argon-filled glovebox. The solution was removed from the glovebox and 7.5 mL of oleic acid surfactant was added and stirred under ambient conditions. To create the reaction slurry, Solutions 1 and 2 were added sequentially to Solution 3

under stirring in open air. The addition of Solution 1 induced a white precipitation due to a rapid change in solubility of the salts, and the addition of Solution 2 resulted in a total reaction mixture at pH 13. The slurry was transferred to a 125 mL teflon-lined autoclave (Parr Instrument Co., No. 4748). The vessel was sealed and placed in an oven, which was ramped to 240 °C at a rate of 4 °C/min. The time at-temperature was varied from 1-72 hr to evaluate the effect on synthetic outcomes. The vessels were allowed to cool to room temperature; The reaction mixtures were sequestered, and products washed with ethanol three times, which were collected by centrifugation. The resulting white powders were allowed to dry in an oven at 80 °C overnight. Separate sets of optimizations were also performed in a set where 60 mL of ethylene glycol replaced the ethanol and oleic acid volumes in the mixture. All samples were labeled according to the solvent choice and oven time (i.e., Et-18 corresponds to the synthetic run within ethanol, held at 240°C for 18hr). A full sample code with description (**Table 1**) is available in the Discussion Section.

Phase identification was performed via XRD with a Bruker D8 Advance under Bragg-Brentano geometry, Cu K_{α} radiation ($K_{\alpha l} = 1.5406$ Å, $K_{\alpha 2} = 1.5444$ Å) at 40 kV and 40 mA. Coupled-2 θ angles varied from 10-85° at 0.01°/step with exposure time of 0.850 s. For certain samples, synchrotron diffraction ($\lambda = 0.459029$ Å) was necessary to elucidate composition changes with reaction time, which was completed at Sector 11-BM within the Advanced Photon Source at Argonne National Laboratory. To confirm phase identity and purity, Rietveld Refinements were executed using the GSAS-II software package.⁶³ The size and shape of samples was evaluated via Transmission Electron Microscopy (TEM) using a JEOL-3010 microscope operating at 300 kV on 400-mesh lacey carbon copper-backed grids (Ted Pella Inc.) in a bright field configuration. Lastly, local lithium environments were probed for select samples via ⁷Li Magic Angle Spinning Nuclear Magnetic Resonance (MAS-NMR) Spectroscopy using a Bruker Avance-III 400 NMR spectrometer and 1.9 mm Bruker HXY MAS probe with a spinning rate of 20.0 kHz.

Results and Discussion

For the synthesis of $\text{Li}_{3x}\text{La}_{2/3-x}$ \square $_{1/3-2x}\text{TiO}_3$, the reaction conditions were altered to influence the composition of the final product, whereas the choice of solvent and surfactants was used to tune the particle size and morphology. First, attention is paid to the samples prepared in the mixture of ethanol, where oleic acid was used as the surfactant. Laboratory XRD is presented in Figure 2a for these samples presented alongside synchrotron diffraction data of the sample Et-18 (Figures S3-4). Note the general peak broadening in all compounds is indicative of fine nanomaterials, as noted in select TEM images (Figure 2b), where most particles displayed at least one dimension of 100 nm or shorter. Early formation of a cubic perovskite phase (Pm-3m, PDF# 00-046-0465) was noted in as little as one hour at temperature, accompanied by a hexagonal La(OH)₃ impurity (P6₃/m, PDF# 01-079-539), which is favored to form in basic conditions in the presence of water. ^{64, 65} With increased reaction time between 6 and 36 hr, the XRD patterns indicated that the cubic perovskite phase became the dominant product, and appeared to be nearly chemically pure by the XRD. There was nearly no meaningful variation with crystal lattice parameters found for these samples with time, indicating the dopant concentrations were consistent (Table 1), and correlated to the retention of the cubic phase. A calibration line was constructed from literature values of Li concentration from diffraction data (Figure S1), which were compared to mass spectra that report titanium and oxygen on-stoichiometry. 21, 66-⁷² Using this calibration line, we were able to estimate Li_{3x}La_{2/3-x} $\prod_{1/3-2x}$ TiO₃ to be around x ~ 0.1, as expected for cubic structures. This outcome highlights the unique access to the cubic phase in a solution synthesis, despite being metastable at such low temperature, which is similar to the synthetic observations of related titanium oxides. 53, 54, 57, 59, 73 The phase composition of LLTO in this synthetic environment only shows a weak dependence on oven time at this temperature, implying that Li⁺ and La³⁺ can incorporate simultaneously into the TiO₆²⁻ backbone.

Table 1. Crystal parameters extracted from fits of the XRD patterns for all samples in this article. Samples are color-coded to show the respective sets. For the glycol powders where distinct splitting was able to be resolved through refinement, two lattice parameters. Phase fractions noted for the EG-based powders were extracted from synchrotron XRD patterns.

Ethanol / Oleic Acid									
Sample Code	Crystal Parameter (Å)	Wt. Fractions	Crystallite Size (nm)	Extrapolated x	Extrapolated Stoich.				
Et-72	<i>a</i> = 3.867(4), <i>c</i> = 7.734(5)	-	23	0.13(8)	$Li_{0.41}La_{0.53} \textstyle \bigsqcup_{0.06} TiO_3$				
Et-48	3.888(5)	-	23	0.068(4)	$Li_{0.22}La_{0.59} \square_{0.19} TiO_3$				
Et-36	3.882(6)	-	27	0.084(7)	$\text{Li}_{0.27}\text{La}_{0.58}\square_{0.15}\text{TiO}_3$				
Et-30	3.884(5)	-	22	0.078(5)	$\text{Li}_{0.26}\text{La}_{0.58} \square_{0.16} \text{TiO}_3$				
Et-24	3.879(2)	-	23	0.095(3)	$\text{Li}_{0.31}\text{La}_{0.56} \square_{0.13}\text{TiO}_3$				
Et-18	3.872(8)	-	22	0.11(1)	Li _{0.36} La _{0.55} \square 0.09TiO ₃				
Et-12	3.879(3)	-	22	0.095(0)	Li _{0.31} La _{0.56} \square _{0.13} TiO ₃				
Et-6	3.881(9)	-	20	0.086(3)	$\text{Li}_{0.28}\text{La}_{0.57} \square_{0.15}\text{TiO}_3$				
Et-1	3.884(7)	-	25	0.078(5)	$\text{Li}_{0.26}\text{La}_{0.58} \square_{0.16}\text{TiO}_3$				
Ethylene Glycol									
Sample Code	Crystal Parameter (a, \mathring{A})	Wt. Fractions	Crystallite Size (nm)	Extrapolated x	Extrapolated Stoich.				
EG-72	3.901(4)	-	1,000	0.033(4)	$\text{Li}_{0.11}\text{La}_{0.63} \square_{0.26}\text{TiO}_3$				
EC 19	3.888(1)	0.12	890	0.043(2)	$\text{Li}_{0.23}\text{La}_{0.59} \square_{0.18}\text{TiO}_3$				
EG-18	3.901(8)	0.88		0.032(1)	$Li_{0.11}La_{0.63} \square_{0.26} TiO_3$				
EG-15	3.886(1)	0.35	780	0.075(0),	$\text{Li}_{0.25}\text{La}_{0.58} \square_{0.17}\text{TiO}_3$				
	3.901(0)	0.65	, , ,	0.035(3)	$Li_{0.11}La_{0.63} \square_{0.26} TiO_3$				
EG-12	3.878(4)	-	360	0.097(3)	$\text{Li}_{0.32}\text{La}_{0.56}$ $\square_{0.12}\text{TiO}_3$				
	3.889(4)	-		0.068(2)	$\text{Li}_{0.22}\text{La}_{0.59} \square_{0.19}\text{TiO}_3$				
EG-9	3.883(0)	0.46	150	0.084(4)	$\text{Li}_{0.27}\text{La}_{0.58} \square_{0.15}\text{TiO}_3$				
	3.893(3)	0.54		0.057(5)	$Li_{0.19}La_{0.60} \square_{0.21} TiO_3$				
EG-3	3.884(0)	0.47	3	0.081(2)	$Li_{0.26}La_{0.58} \square_{0.16} TiO_3$,				
	3.897(8)	0.53		0.043(3)	$\text{Li}_{0.14}\text{La}_{0.62} \square_{0.24} \text{TiO}_3$				
EG-1.5	3.892(1)	-	2	0.059(4)	$\text{Li}_{0.19}\text{La}_{0.60} \square_{0.20}\text{TiO}_3$				
	3.899(4)	-	<u> </u>	0.041(1)	$Li_{0.13}La_{0.62} \square_{0.25} TiO_3$				
EG-1	3.887(8)	0.53	2	0.070(5)	$\text{Li}_{0.23}\text{La}_{0.59}$ $\square_{0.18}\text{TiO}_3$				
	3.900(3)	0.47		0.038(7)	$\text{Li}_{0.12}\text{La}_{0.63} \square_{0.25}\text{TiO}_3$				

Interestingly, a large change in composition was observed for the Et-72 sample. The complex pattern was indexed with the tetragonal (P4/mmm, PDF # 00-87-0935) polymorph of the perovskite, primarily identified from the two superstructural peaks labelled in the diffractogram, at 12.16° and 25.27°. Other peaks that overlap with the parent cubic symmetry were not superimposed in the lattice positions in **Figure 2a** for sake of clarity. Refinement of this pattern is presented in the **Supporting Information** (**Figure S4**). Traditionally, cubic structures tend to contain more lanthanum than the tetragonal, implying the longer oven

times result in an increase of lithium concentrations, limiting a-site vacancies. This suggests that the ordering of the dopants to form the tetragonal superstructure was limited in the lower oven times, and this threshold was surpassed between 36 and 72hr. This formation was accompanied by both cubic LiTiO₂ (Fm-3m, PDF# 01-079-539) and a hydrous lithium titanate (Li_{1.81}H_{0.19})Ti₂O₅·2H₂O (Cmmm, PDF# 00-047-0123) which have been synthesized hydrothermally in similar conditions (**Figure S5**). S8, 74 For all samples, the lattice parameter showed very small variations at different reaction times, without any obvious trend for the cubic phases (**Table 1**). A calibration line was constructed from literature values of Li concentration from diffraction data, which were compared to mass spectra that report titanium and oxygen onstoichiometry. Using this calibration line, we were able to estimate Li_{3x}La_{2/3-x} \Box 1/3-2xTiO₃ to be around $x \sim 0.1$, as expected for cubic structures.

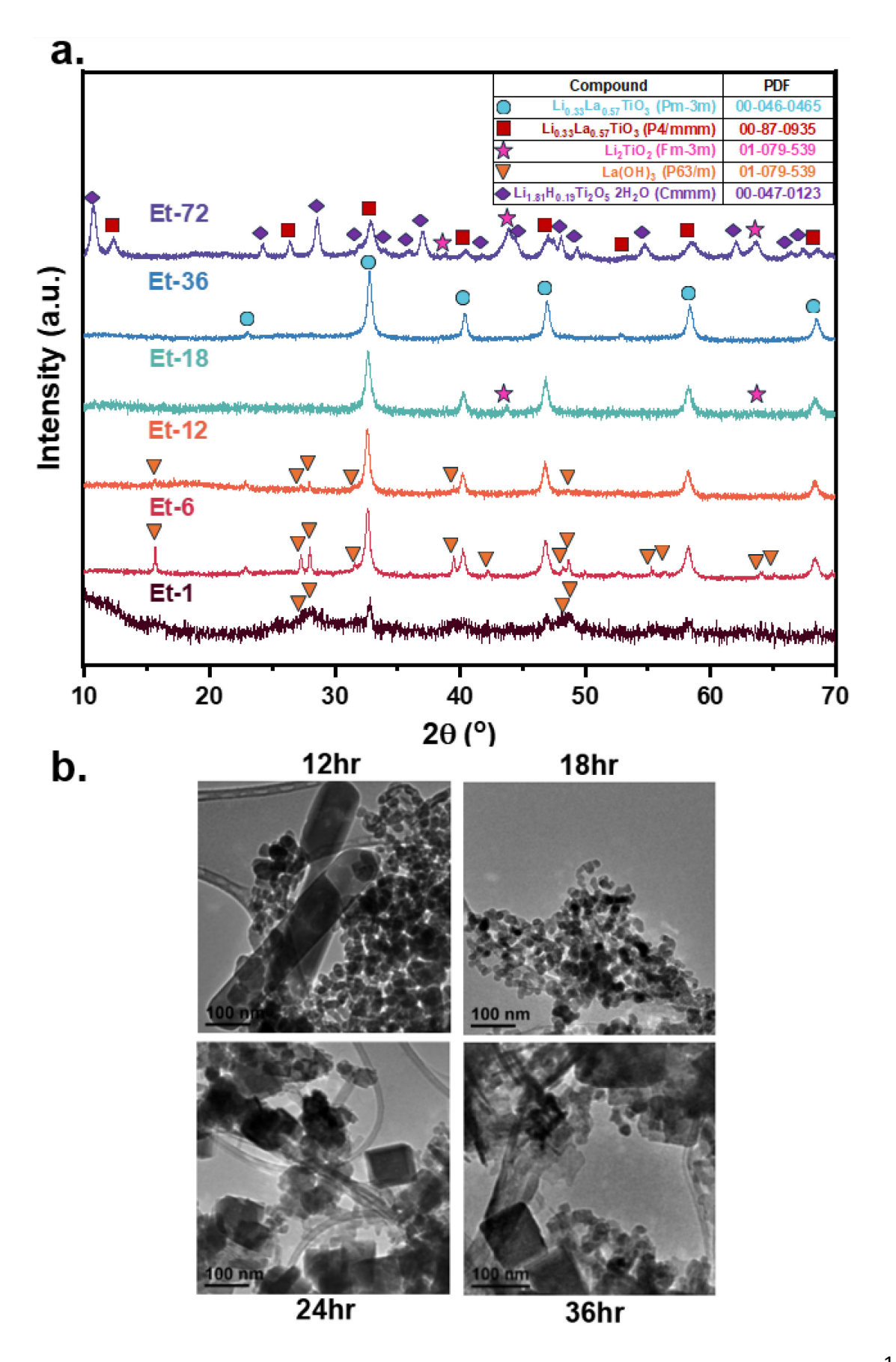


Figure 2. a. XRD patterns of c-LLTO powders prepared in an ethanol/oleic acid environment with times varied from 1 to 72hr. **b.** Indicative TEM images of samples Et-12, 18, 24, and 36, depicting various particle sizes and shapes. The cubic $Li_{3x}La_{2/3-x}TiO_3$ phase was only indexed in the Et-36 sample and is present in every other sample at a lower time.

For cases where dynamics of lithium environment and Li-ion conductivity are aimed to be established, it aids in targeting samples with a monodisperse morphology. Generally, particle size and homogeneity were highest for Et-18, showing nanocrystals of ~20 - 25 nm (**Figure 2b**). Comparisons of the crystallite size from pattern fitting (**Table 1**) suggest the nanoparticle sizes on average were consistent regardless of reaction time. This morphology is consistent with the formation of micelle or reverse micelle liquid structures at elevated pressures, ^{75, 76} where particle growth velocity is limited greatly by diffusion. TEM images suggest the formation of a somewhat heterogeneous morphology in early reaction times, where the observed large, faceted nanorods would be consistent with the presence of the La(OH)₃ impurity phase. ^{64, 65} At longer timescales, a heterogeneous morphology is observed despite the chemistry being clean, depicting larger and more diverse shapes of LLTO present.

To explore the robustness of the synthetic method, both the solvent and the surfactant were swapped simultaneously for equal volumes ethylene glycol (EG). In the literature, the polar glycol has been identified as an excellent solvent and directing agent in colloidal syntheses. 77-79 XRD and representative TEM images are presented in **Figure 3 along with refined synchrotron diffraction of select EG-xx samples in Figures S6-S10.** In the EG-based runs, the formation of c-LLTO was noted in as little as 1 hour of synthesis, and the size of the nanocrystals was particularly small, with diameters near or below 10 nm. An apparent shoulder was observed near 40° in the sample EG-1 (**Figure 3a**), which could initially be taken as indicating the presence of a secondary Li_xTiO₂ in a very low concentration. 80,81. However, this peak was not observed in the synchrotron diffraction pattern of the same sample (**Figure S10**) or in the subsequent diffraction patterns of other samples, suggesting it may be a noise artifact, and, thus, not important in the overall phase stabilization of c-LLTO (**Figure S10**).

Compared with the ethanol/oleic acid environment, a c-LLTO phase is clearly the dominant product across a more robust timescale. It was observed that phase purity was obtained for the set of Et-xx, and a biphasic evolution was noted to take place on a faster timescale when ethylene glycol was used as solvent/surfactant.^{59, 78, 79, 82} Interestingly, the TEM images of the EG-xx set depict the size evolution of particulate which quickly crystallizes into sizes that exceed several hundred nanometers. It is evident that the particles form agglomerations and collect to form the larger monocrystalline structures noted anywhere after 3 hours at-temperature. As the particles are allowed to collect and reform more quickly, the result is the production of much thicker, highly faceted particles. The Scherrer analyses of these patterns suggest a large increase in crystallite size with reaction time (**Table 1**), consistent with TEM observations.

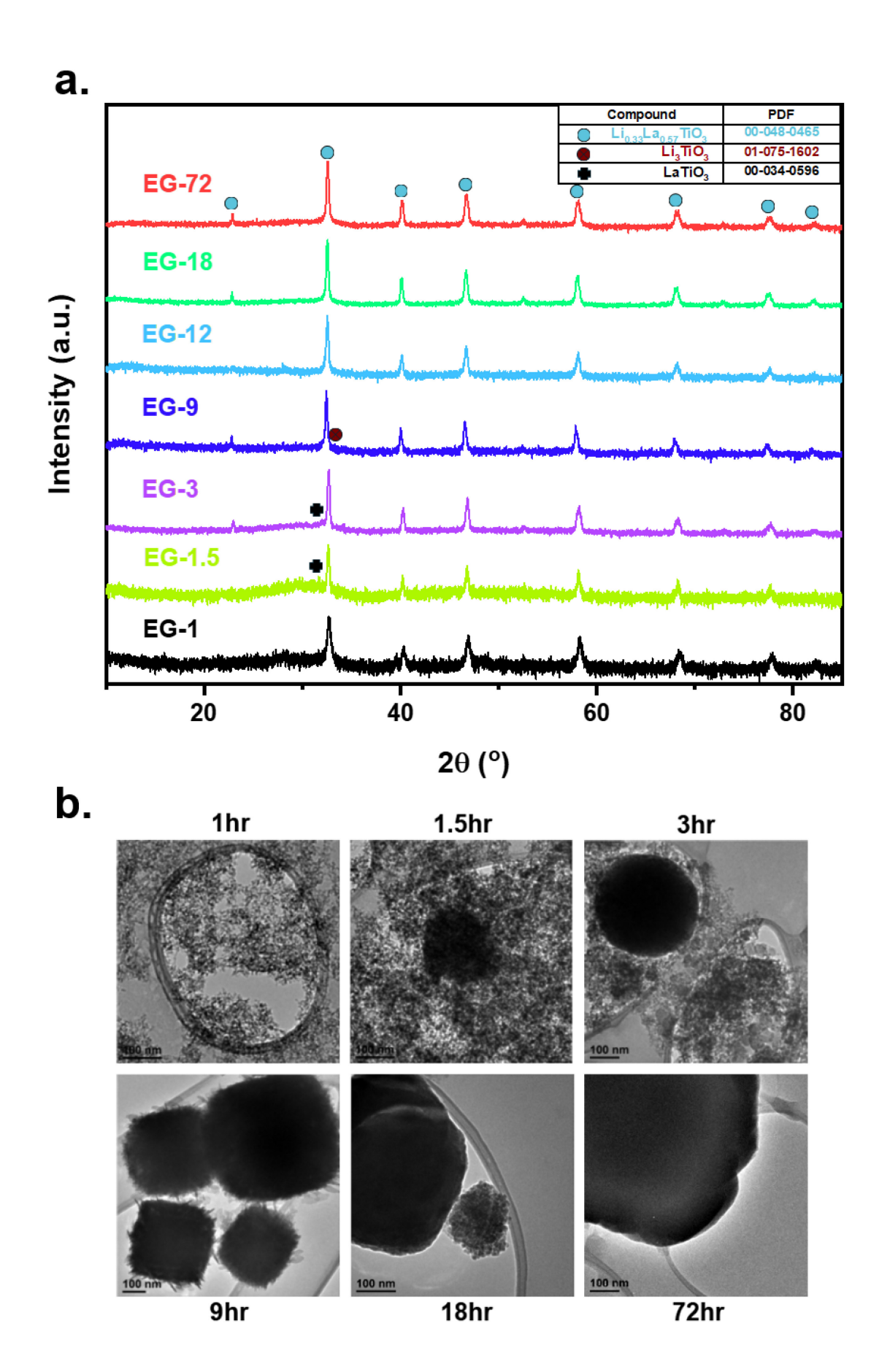


Figure 3. a. Powder X-ray Diffraction patterns of c-LLTO powders prepared in an EG environment, times varied from 1-72hr. **b.** Representative TEM images of samples EG-1, 1.5, 3, 9, 18, and 72. The cubic Li_{3x}La_{2/3-x}TiO₃ phase was only indexed for the c-LLTO phase for one sample, EG-72.

While the formation of c-LLTO in these systems happens faster, with increased ability to tune particle shape and size, XRD suggested that there is the stabilization of two, unique crystal phases that could be indexed with a cubic lattice of the same symmetry as LLTO. The presence of these lattices was more easily discerned from synchrotron XRD data (**Figure 4**) in a Debye Scherrer geometry, in the form of splitting of all peaks. A phase transition to tetragonal or orthorhombic structures based on the parent Pm-3m would not split the (111) crystallographic direction. Thus, corresponding Rietveld fits of the patterns were used to extract cell parameters and weight fractions, presented in the **Figures S6-10**. As noted in the Experimental Section, select powders were examined via synchrotron radiation, but only those made in EG displayed evidence of multiple phases, so they are the only ones for which phase fractions were reported in **Table 1**. The early evolution at 1hr of a smaller crystal lattice parameter (3.887(8) Å, higher angle 20 peak envelope) was observed in a nearly even concentration with a larger lattice parameter (3.900(3) Å). As time increased, the nucleation and growth of the larger crystal parameter was favored over the smaller one. This may have several implications for the phase stability of the cubic titanate in these conditions.

Examining the self-diffusion of cations in these slurries may be an interesting follow-up to correlate cationic mobility and influence on the final composition of the titanate crystallized. In contrast, during the reaction, it is evident that there is an apparent reorganization of elements as the reaction proceeds, since the different cell parameters was assumed to represent distinct Li/La ratios based on the literature. $^{21, 66-72}$ Specifically, the time-dependent evolution of the larger crystal parameter is associated with slightly higher lanthanum content over the lithium in the $\text{Li}_{3x}\text{La}_{2/3-x}$ $\text{Im}_{3/2-2x}\text{Li}_{3/2-2x}$ $\text{Li}_{3/2-2x}\text{Li}_{3/2-2x}$ $\text{Li}_{3/2-2x}\text{Li}_{3/2-2x}$

method. Follow-up work is necessary to verify this hypothesis. The growth of the larger crystals at longer reactions times implies transition between two cubic lattices as more lanthanum incorporates.

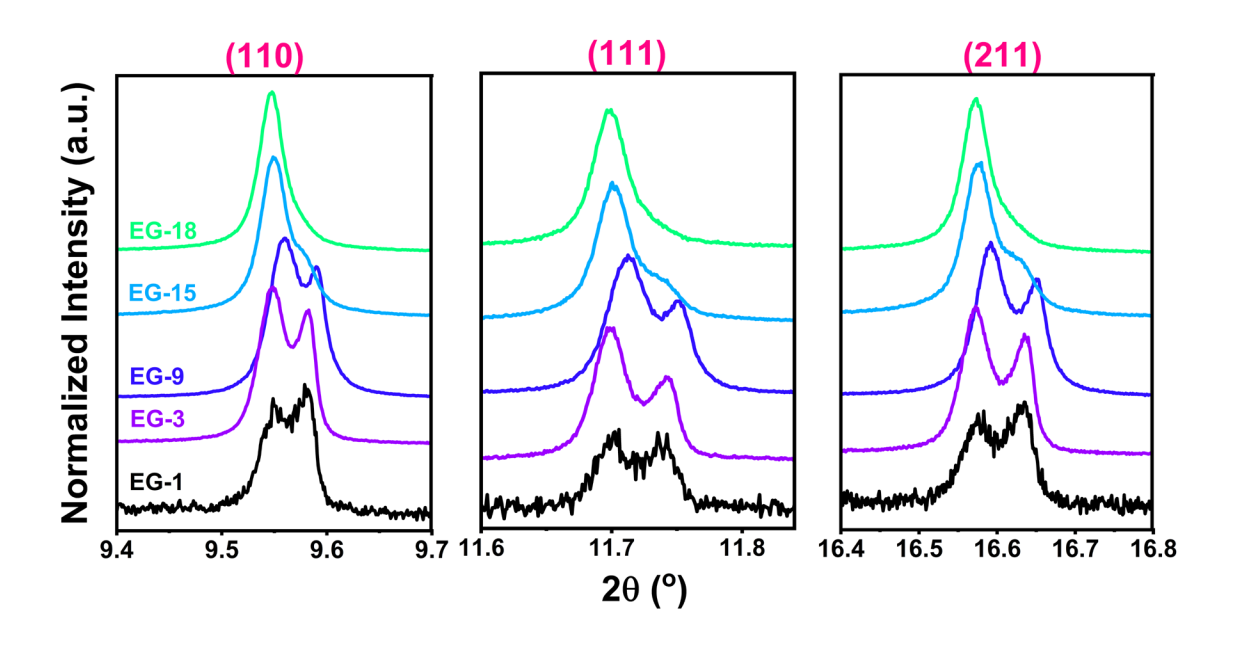


Figure 4. Synchrotron XRD patterns of c-LLTO powders prepared in an EG environment with times varied from 1-18hr. Plots denote the (110), (111), and (211) peaks from left to right, which denote consistent peak ratios, which are consistent with two unique cubic phases. Rietveld Refinement data for all samples depicted can be found in Figures **S6-S10**.

Different techniques have been used to probe the location of lithium ions within the lattice of LLTO; however, these are often limited by the small size and low Z value of Li⁺. To examine the relative changes in lithium environments across different synthetic environments, solid-state ⁷Li (I = 3/2) MAS NMR spectra were taken for samples Et-18, EG-18, and EG-1, as shown in **Figure 5**. MAS spectra were collected at 20 kHz in efforts to reduce the effects of anisotropic line shapes, producing more easily deconvoluted central peaks. All samples had high intensities, proving the incorporation of Li⁺ into the samples. Clearly, there were large relative differences in the spectra, inferring that modulating the synthetic method, in turn, imparted LLTO compositions with different local lithium environments.

The ultrafine nanoparticles of several nm in diameter in EG-1 led to a striking spectral broadening with the resonance centered about 1.43 ppm. This observation suggests that Li⁺ is not only incorporated into the lattice, but it does so in highly disordered arrangements, given the width of the peak. This broadening of the spectra went along with as a lower s/n ratio. Sample Et-18 had slightly larger particles and presented two components centered at 0.25 and 0.17 ppm, corresponding to two unique A-site Li contributions. In this synthetic environment, the two lithium have quite different FWHM (**Table 2**) values, implying the signal relaxations are quite different within the same phase. The much larger crystals of EG-18 led to spectra that had similar aspects, but with slight changes in their position: one environment shifted to a higher chemical shift (Li 1, 0.88 ppm) and the other to a lower chemical shift (Li 2, -1.68 ppm). Since there are two unique cubic phases in these samples, it is currently not possible to suggest the origin of these shifts concretely. However, since Et-18 was suggested to be one phase, the existence of two lines in the other samples may not have their origin in the small phase differences evidenced by diffraction. Given the sensitivity of the ⁷Li nucleus, the relative changes in peak positions are quite minor, as only small shifts in the central ±1/2 transition have been reported for various phases and therefore dopant concentrations in the literature.

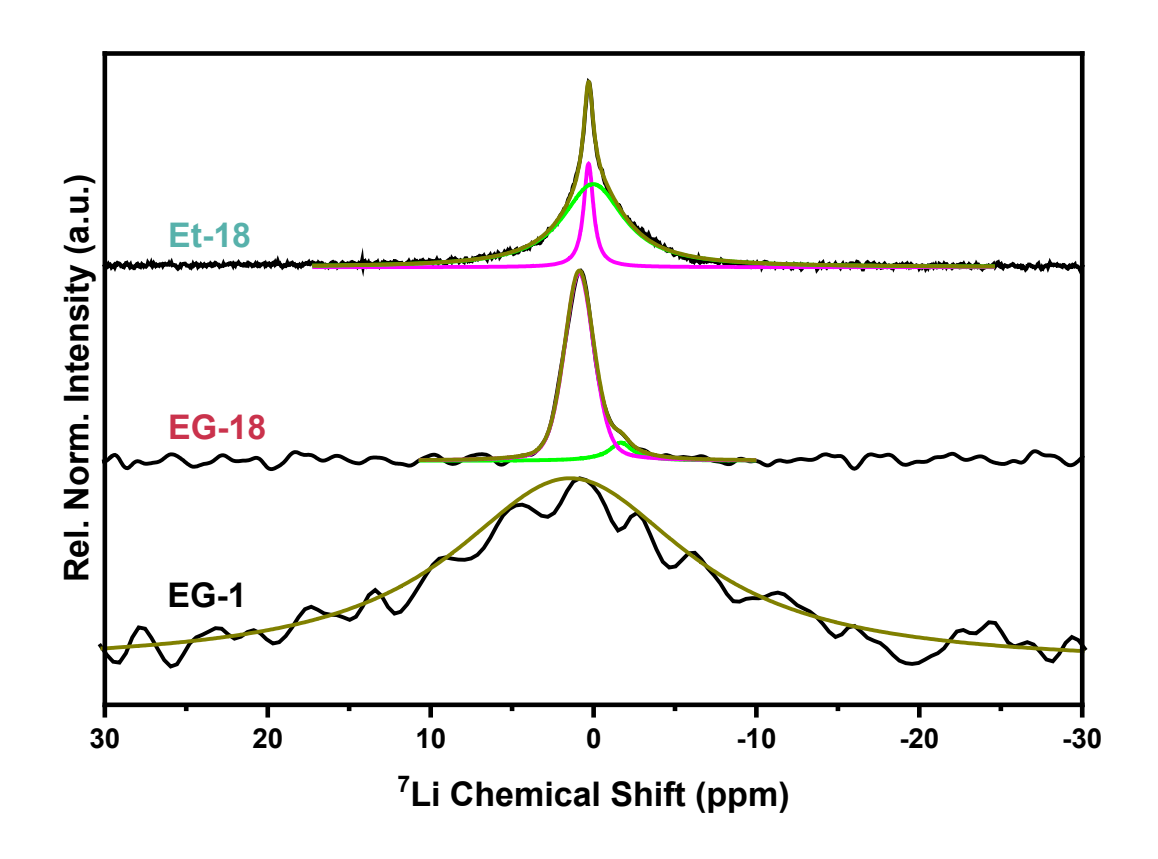


Figure 5. ⁷Li NMR MAS spectra of the samples Et-18, EG-18, and EG-1 powders taken at 294 K, collected at 116.64 MHz with a 20 kHz spin rate. Reconstructions of the spectra for their principal components may be found in the Figures S11-13.

Sample	Component	Position, δ (ppm)	<i>FWHM, ∆ (ppm)</i>	%
Et-18	Li 1	0.25	0.90	23
	Li 2	0.17	4.98	76
EG-18	Li 1	0.88	1.42	90
	Li 2	-1.68	1.88	10
EG-1	Li 1	1.43	17.9	100

Table 2. Spectral deconvolution parameters for the reconstruction of the ⁷Li MAS NMR spectra shown in **Figure 5.**

Previous descriptions of similar LLTO compositions via NMR have been made for samples that vary in terms of bulk phase and particle size.^{83-85, 87} Many interpretations have been made in the literature, and may be used to describe MAS spectra of LLTO compounds presented here. According to Bohnke *et al.*,⁸³ asymmetry in MAS spectra for LLTO may be attributed to describe disorder at the A-site with a distribution of activation energies for 3-D motion for a c-LLTO polycrystal synthesized via a traditional

solid state reaction. This assumes that the vacancy and lanthanum concentrations about an individual Asite is not ordered, and that Li⁺ does not necessarily occupy the ideal crystallographic position precisely. These observations did not aim to address potential impacts of domain size on spectral features, however. It has been shown in cross-polarization HETCOR studies that nano-sized LLTO prepared via a solution-gelation method after a lithium/proton exchange in acid exhibits a motion-limited lithium environment with a large FWHM near the surface sites in a c-LLTO particle through confinement.⁸⁵

It was likely both relative disorder and particle size may impact the observed differences of the MAS and can be true simultaneously. To evaluate the lithium dynamics for these samples, T_l relaxation measurements are presented in Figure 6 and summarized by Table 3. The dynamics measured were all fitted with two relaxation components (one-component attempts are available in Figures S14-16). suggesting that there are two types of lithium relaxations in these samples. This agrees with the MAS, where the samples Et-18 and EG-18 are deconvoluted to show two domains each. This could either be due to differences between the chemistry in the phases, or the morphologies associated with each synthetic run. The XRD revealed that the Et-xx samples were composed of a single cubic phase, functionally ruling phase identity as the determinant for relaxometry components. Therefore, local Li⁺ environments are associated more closely with changes in morphology as opposed to the biphasic nature of the EG-xx samples. The relative percentages of the components for the T_I match quite well to that of the MAS. For instance, the narrow component in the MAS spectra of Et-18 (FWHM = 0.90 ppm, 23%) matches well in relative percentage to the faster recovery dynamic in the relaxation (~ 0.29 s, 22%). The same is true for each component of the deconvolution. In the case of EG-1, it may be either that the small size of the particles or a larger relative disorder contribute to a wide FWHM making the individual environments indistinguishable by the MAS spectra, but still presents relaxation values which can be decoupled. Additionally, there is also a faster relaxation dynamic in the EG-18 samples, which are also the largest crystals by several orders of magnitude compared to EG-1 or Et-18, based on TEM presented in Figures 2b and 3b. There is a general trend that the smallest particles tend to have the slowest

relaxation kinetics. While not causal, there is reasonable evidence to suggest that both particle size and the kinetics of lithium relaxation are likely impacting the observed differences in the MAS spectra. This does not, however, rule out local disorder differences between the three samples, which may also be impacted by particle size itself. As grains increase in size, the ratio of surface sites to the bulk of the grain gets smaller necessarily, implying that the small EG-1 particles contain the highest surface fraction, and the large EG-18 particles with the least. It follows that EG-1 particles displayed broader MAS spectra and slower relaxation times, and as the relaxation for the larger particles decreased, so did the broad component of the MAS. These data imply that while nanoparticles are better dispersed in solvents (Figure S2) and allow for the fabrication of hybrid electrolytes more easily, there is highly likely a tradeoff for interfacial ionic conductivities which may limit functionality. Currently, explorations of utilizing these materials in functionalized hybrid electrolytes with polymer matrices are underway.

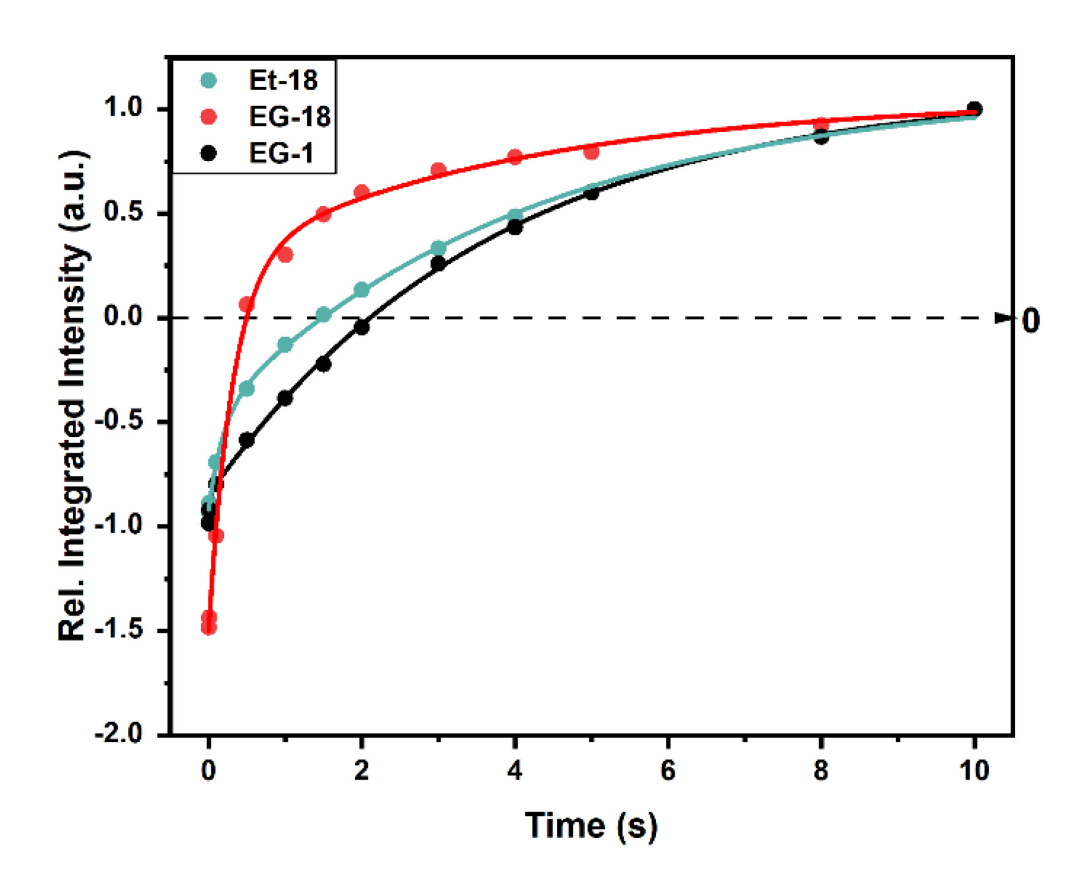


Figure 6. ⁷Li T₁ inversion recovery method to probe the dynamics of the samples Et-18, EG-18, and EG-1 taken at 294 K.

Sample	Component	Relaxation (s)	%	R^2	χ^2
Et-18	Li 1	0.29 ± 0.03	78.0 ± 1	0.9992	4.01*10-4
	Li 2	3.8 ± 0.03	22.0 ± 2	0.9992	
EG-18	Li 1	0.17 ± 0.03	84 ± 1	0.9995	1.75*10-4
	Li 2	2.9 ± 0.4	16 ± 1	0.9993	
EG-1	Li 1	0.39 ± 0.09	52 ± 1	0.9988	3.82*10-4
	Li 2	4.4 ± 0.09	48 ± 1	0.9988	

Table 3. Fit parameters for the reconstruction of the ${}^{7}\text{Li T}_{1}$ dynamics shown in **Figure 6.**

Conclusion

A single-step solvothermal protocol was developed for the synthesis of the cubic perovskite of the composition Li_{3x}La_{2/3-x} $\square_{1/3-2x}$ TiO₃. This work highlights the importance of solvent and surfactant choice when targeting a monodisperse and chemically pure sample. By choosing ethylene glycol as a solvent and surfactant, a much faster rate of crystallization and crystal growth was observed with enhanced control over particle morphology as compared to a system based on ethanol/oleic acid. This observation came at the expense of purity, with the stability of two unique cubic chemistries implying a complex stabilization process. This is an important feature not previously reported and implies that the phase stability is not only achieved by relative metal concentrations, but also the mechanisms of crystal growth employed in each synthetic method. By ⁷Li SS-NMR, it was revealed that decreasing particle size was associated with broader MAS peaks and slower corresponding relaxation dynamics found through T₁ measurements. The framework presented suggests that metastable oxides like LLTO are accessible by solution processing at much lower temperatures than by solid-state synthetic methods, offering unique control over the shape and size of resulting crystals.

Associated Content

Supporting Information

Other supporting data includes calibration lines for dopant concentrations, suspensions of the various perovskites, and detailed XRD fitting information. This material is available free of charge via the Internet at http://pubs.acs.org.

Acknowledgements

This work was supported through the Division of Chemical, Bioengineering, Environmental and Transportation Systems of the National Science Foundation (grant no. 2022723). TEM measurements were conducted in the Electron Microscopy Core of the Research Resource Center, which is housed within the University of Illinois Chicago. Synchrotron XRD of select samples was performed at Sector 11-BM at the Advanced Photon Source within Argonne National Laboratory.

Author Information

Michael A. Dato – Department of Chemistry, University of Illinois Chicago, Chicago, IL 60607, USA. https://orcid.org/0000-0002-1719-6711

Linhua Hu – Department of Chemistry, University of Illinois Chicago, Chicago, IL 60607, USA. http://orcid.org/0000-0002-0177-3983

Dan McElheny – Department of Chemistry, University of Illinois Chicago, Chicago, IL 60607, USA.

Jordi Cabana – Department of Chemistry, University of Illinois Chicago, Chicago, IL 60607, USA. https://orcid.org/0000-0002-2353-5986

Corresponding Authors

*E-mail: jcabana@uic.edu

Conflicts of Interest

There are no conflicts of interest to declare.

References

- (1) Trahey, L.; Brushett, F. R.; Balsara, N. P.; Ceder, G.; Cheng, L.; Chiang, Y. M.; Hahn, N. T.; Ingram, B. J.; Minteer, S. D.; Moore, J. S.; et al. Energy Storage Emerging: A Perspective from the Joint Center for Energy Storage Research. *Proc. Natl. Acad. Sci. USA* **2020**, 117, 12550-12557.
- (2) Wang, Q.; Lu, Y.; Jin, J.; Chen, C.; Wen, Z. Li1.5al0.5ge1.5(Po4)3 Ceramic Based Lithium-Sulfur Batteries with High Cycling Stability Enabled by a Dual Confinement Effect for Polysulfides. *ChemElectroChem* **2020**, 7, 4093-4100.
- (3) Liu, K.; Liu, Y.; Lin, D.; Pei, A.; Cui, Y. Materials for Lithium-Ion Battery Safety. Sci. Adv. 2018, 4, 1-11.
- (4) Zhang, L.; Zhang, X.; Tian, G.; Zhang, Q.; Knapp, M.; Ehrenberg, H.; Chen, G.; Shen, Z.; Yang, G.; Gu, L.; et al. Lithium Lanthanum Titanate Perovskite as an Anode for Lithium Ion Batteries. *Nat. Commun.* **2020**, 11, 1-8.

- (5) Xia, H.; Chen, Y.; Wu, J.; Shao, S.; Chen, G.; Zhang, H.; Dai, Q.; Wang, X. Oxidative Decomposition of Chlorobenzene over Iron Titanate Catalysts: The Critical Roles of Oxygen Vacancies and Adsorption Geometries. *Appl. Catalysis A: General* **2021**, 617, 118118.
- (6) Gupta, A. K.; Gupta, S.; Sachan, R. Laser Irradiation Induced Atomic Structure Modifications in Strontium Titanate. *Jom* **2021**, 74, 143-150.
- (7) Arsenyev, P. A.; Tkachuk, G. N. Spectroscopic and Laser Properties of Neodymium Doped Yttrium Titanate Crystals. *J. Appl. Spec.* **2020**, 86, 1045-1047.
- (8) Farhadi, N.; Tabatabaie, T.; Ramavandi, B.; Amiri, F. Optimization and Characterization of Zeolite-Titanate for Ibuprofen Elimination by Sonication/Hydrogen Peroxide/Ultraviolet Activity. *Ultrason. Sonochem.* **2020**, 67, 105122.
- (9) Xiao, J. How Lithium Dendrites Form in Liquid Batteries. Sci. 2019, 366, 426-427.
- (10) Li, T.; Bai, X.; Gulzar, U.; Bai, Y. J.; Capiglia, C.; Deng, W.; Zhou, X.; Liu, Z.; Feng, Z.; Proietti Zaccaria, R. A Comprehensive Understanding of Lithium–Sulfur Battery Technology. *Adv. Func. Mater.* **2019**, 29, 1-56.
- (11) Murugan, R.; Thangadurai, V.; Weppner, W. Fast Lithium Ion Conduction in Garnet-Type Li₇la₃zr₂o₁₂. *Angew. Chem. Int. Ed. Engl.* **2007**, 46, 7778-7781.
- (12) Canepa, P.; Dawson, J. A.; Sai Gautam, G.; Statham, J. M.; Parker, S. C.; Islam, M. S. Particle Morphology and Lithium Segregation to Surfaces of the Li₇la₃zr₂o₁₂ Solid Electrolyte. *Chem. Mater.* **2018**, 30, 3019-3027.
- (13) Subramanian, K.; Alexander, G. V.; Karthik, K.; Patra, S.; Indu, M. S.; Sreejith, O. V.; Viswanathan, R.; Narayanasamy, J.; Murugan, R. A Brief Review of Recent Advances in Garnet Structured Solid Electrolyte Based Lithium Metal Batteries. *J. Ener. Storage* **2021**, 33, 102157.
- (14) Thangadurai, V.; Weppner, W. Solid State Lithium Ion Conductors: Design Considerations by Thermodynamic Approach. *Ionics* **2002**, 8, 281-292.
- (15) Jonderian, A.; Ting, M.; McCalla, E. Metastability in Li–La–Ti–O Perovskite Materials and Its Impact on Ionic Conductivity. *Chem. Mater.* **2021**, 33, 4792-4804.
- (16) Jonderian, A.; McCalla, E. The Role of Metal Substitutions in the Development of Li Batteries, Part Ii: Solid Electrolytes. *Mater. Adv.* **2021**, 2, 2846-2875.
- (17) Bohnke, O.; Duroy, H.; Fourquet, J. L.; Ronchetti, S.; Mazza, D. In Search of the Cubic Phase of the Li⁺ Ion-Conducting Perovskite La_{2/3-X}li_{3x}tio₃: Structure and Properties of Quenched and in Situ Heated Samples. *Sol. State Ionics* **2002**, 149, 217-226.
- (18) Guo, X.; Maram, P. S.; Navrotsky, A. A Correlation between Formation Enthalpy and Ionic Conductivity in Perovskite-Structured Li_{3x}la_{0.67-X}tio₃ Solid Lithium Ion Conductors. *J. Mater. Chem. A* **2017**, 5, 12951-12957.
- (19) Stramare, S.; Thangadurai, V.; Weppner, W. Lithium Lanthanum Titanates: A Review. *Chem. Mater.* **2003**, 15, 3974-3990.
- (20) Lee, S.-J.; Bae, J.-J.; Son, J.-T. Structural and Electrical Effects of Y-Doped Li_{0.33}la_{0.56-X}y_xtio₃ Solid Electrolytes on All-Solid-State Lithium Ion Batteries. *J. Korean Phys. Soc.* **2019**, 74, 73-77.
- (21) Ibarra, J.; Varez, A.; Leon, C.; Santamaria, J.; Torres-Martinez, L. M.; Sanz, J. Influence of Composition on the Structure and Conductivity of the Fast Ionic Conductors $La_{2/3-X}li_{3x}tio_3$ (0.03 < X < 0.167). Sol. State Ionics **2000**, 134, 219-228.

- (22) Ban, C. W.; Choi, G. M. The Effect of Sintering on the Grain Boundary Conductivity of Lithium Lanthanum Titanates. *Sol. State Ionics* **2001**, 140, 285-292.
- (23) Wang, M. J.; Wolfenstine, J. B.; Sakamoto, J. Mixed Electronic and Ionic Conduction Properties of Lithium Lanthanum Titanate. *Adv. Func. Mater.* **2020**, 30, 1909140.
- (24) Xu, P.; Rheinheimer, W.; Mishra, A.; Shuvo, S. N.; Qi, Z.; Wang, H.; Dongare, A. M.; Stanciu, L. A. Origin of High Interfacial Resistance in Solid-State Batteries: Llto/Lco Half-Cells. *ChemElectroChem* **2021**, 8, 1847-1857.
- (25) Symington, A. R.; Molinari, M.; Dawson, J. A.; Statham, J. M.; Purton, J.; Canepa, P.; Parker, S. C. Elucidating the Nature of Grain Boundary Resistance in Lithium Lanthanum Titanate. *J. Mater. Chem. A* **2021**, 9, 6487-6498.
- (26) Sasano, S.; Ishikawa, R.; Sanchez-Santolino, G.; Ohta, H.; Shibata, N.; Ikuhara, Y. Atomistic Origin of Li-Ion Conductivity Reduction at (Li_{3x}la_{2/3-X})Tio₃ Grain Boundary. *Nano. Lett.* **2021**, 21, 6282-6288.
- (27) Robertson, A. D.; Garcia Martin, S.; Coats, A.; West, A. R. Phase Diagrams and Crystal Chemistry in the Li⁺ Ion Conducting Perovskites, Li_{0.5-3x}re_{0.5+x}tio₃: Re = La, Nd. *J. Mater. Chem.* **1995**, 5, 1405-1412.
- (28) Harada, Y.; Ishigaki, T.; Kawai, H.; Kuwano, J. Lithium Ion Conductivity of Polycrystalline Perovskite La_{0.67}. xlitio with Ordered and Disordered a-Site Ions. *Sol. State Ionics* **1998**, 108, 407-413.
- (29) Catti, M.; Sommariva, M.; Ibberson, R. M. Tetragonal Superstructure and Thermal History of L_{i0.3}la_{0.567}tio₃ (Llto) Solid Electrolyte by Neutron Diffraction. *J. Mater. Chem.* **2007**, 17, 1300-1307.
- (30) Chambers, M. S.; Chen, J.; Sacci, R. L.; McAuliffe, R. D.; Sun, W.; Veith, G. M. Memory Effect on the Synthesis of Perovskite-Type Li-Ion Conductor Li_{3x}la_{2/3-X/3}tio₃ (Llto). *Chem. Mater.* **2024**, 36, 1197-1213.
- (31) Avila, V.; Yoon, B.; Ingraci Neto, R. R.; Silva, R. S.; Ghose, S.; Raj, R.; Jesus, L. M. Reactive Flash Sintering of the Complex Oxide Li_{0.5}la_{0.5}tio₃ Starting from an Amorphous Precursor Powder. *Scri. Mater.* **2020**, 176, 78-82.
- (32) Silva, J. H. L.; Alves, Y. G. S.; Almeida, A.; Agostinho Moreira, J.; Vilarinho, R.; Santos, J. C. A.; Leyet, Y.; Jesus, L. M.; Silva, R. S. Study of the Ionic Conductivity of Li_{0.5}la_{0.5}tio₃ Laser-Sintered Ceramics. *J. Euro. Cer. Soc.* **2020**, 40, 5619-5625.
- (33) Zhang, S.; Zhao, H.; Guo, J.; Du, Z.; Wang, J.; Świerczek, K. Characterization of Sr-Doped Lithium Lanthanum Titanate with Improved Transport Properties. *Sol. State Ionics* **2019**, 336, 39-46.
- (34) Morata-Orrantia, A.; Garcia-Martin, S.; Moran, E.; Alario-Franco, M. A. A New La_{2/3}li_xti_{1-X}al_xo₃ Solid Solution: Structure, Microstructure, and Li⁺ Conductivity. *Chem. Mater.* **2002**, 14, 2871-2875.
- (35) Wu, J. F.; Guo, X. Origin of the Low Grain Boundary Conductivity in Lithium Ion Conducting Perovskites: Li_(3x)La_(0.67-X)Tio₍₃₎. *Phys. Chem. Chem. Phys.* **2017**, 19, 5880-5887.
- (36) Kwon, W. J.; Kim, H.; Jung, K.-N.; Cho, W.; Kim, S. H.; Lee, J.-W.; Park, M.-S. Enhanced Li⁺ Conduction in Perovskite Li_{3x}la_{2/3-X□1/3-2x}tio₃ Solid-Electrolytes Via Microstructural Engineering. *J. Mater. Chem. A* **2017**, 5, 6257-6262.
- (37) Varez, A.; Ibarra, J.; Rivera, A.; Leon, C.; Santamaria, J.; Laguna, M. A.; Sanjuan, M. L.; Sanz, J. Influence of Quenching Treatments on Structure and Conductivity of the Li_{3x}la_{2/3-x}tio₃ Series. *Chem. Mater.* **2003**, 15, 225-232.
- (38) Diktanaitė, A.; Gaidamavičienė, G.; Kazakevičius, E.; Kežionis, A.; Žalga, A. Aqueous Sol-Gel Synthesis, Structural, Thermoanalytical Studies, and Conductivity Properties of Lithium Lanthanum Titanate. *Thermochim. Acta* **2022**, 715, 1-14.

- (39) Zhou, X.; Gao, C.; Wang, D.; Peng, S.; Huang, L.; Yang, W.; Zhang, W.-H.; Gao, X. Revealing the Dominant Factor of Domain Boundary Resistance on Bulk Conductivity in Lanthanum Lithium Titanates. *J. Energy Chem.* **2022**, 73, 354-359.
- (40) Inaguma, Y.; Liquan, C.; Itoh, M.; Nakamura, T.; Uchida, T.; Ikuta, H.; Wakihara, M. High Ionic Conductivity in Lithium Lanthanum Titanate. *Sol. State Commun.* **1993**, 86, 689-693.
- (41) Belous, A. G.; Novitskaya, G. N.; Polyanetskaya, S. V.; Gornikov, Y. I. Investigation into Complex Oxides of La_{2/3-X}li_{3x}tio₃ Composition. *Russian J. Inorg. Chem.* **1987**, 32, 156-157.
- (42) Yan, S.; Yim, C.-H.; Pankov, V.; Bauer, M.; Baranova, E.; Weck, A.; Merati, A.; Abu-Lebdeh, Y. Perovskite Solid-State Electrolytes for Lithium Metal Batteries. *Batteries* **2021**, 7, 75-95.
- (43) Uhlmann, C.; Braun, P.; Illig, J.; Weber, A.; Ivers-Tiffée, E. Interface and Grain Boundary Resistance of a Lithium Lanthanum Titanate (Li_{3x}la_{2/3-x}tio₃, Llto) Solid Electrolyte. *J. Power Sources* **2016**, 307, 578-586.
- (44) Zhu, L.; Zhu, P.; Fang, Q.; Jing, M.; Shen, X.; Yang, L. A Novel Solid Peo/Llto-Nanowires Polymer Composite Electrolyte for Solid-State Lithium-Ion Battery. *Electrochim. Acta* **2018**, 292, 718-726.
- (45) Patel, V.; Dato, M. A.; Chakraborty, S.; Jiang, X.; Chen, M.; Moy, M.; Yu, X.; Maslyn, J. A.; Hu, L.; Cabana, J.; et al. Cycling of Block Copolymer Composites with Lithium-Conducting Ceramic Nanoparticles. *Front. Chem.* **2023**, 11, 1-13.
- (46) Dawson, J. A.; Canepa, P.; Clarke, M. J.; Famprikis, T.; Ghosh, D.; Islam, M. S. Toward Understanding the Different Influences of Grain Boundaries on Ion Transport in Sulfide and Oxide Solid Electrolytes. *Chem Mater* **2019**, 31, 5296-5304.
- (47) Huang, Z.; Chen, L.; Huang, B.; Xu, B.; Shao, G.; Wang, H.; Li, Y.; Wang, C. A. Enhanced Performance of Li_{6.4}la₃zr_{1.4}ta_{0.6}o₁₂ Solid Electrolyte by the Regulation of Grain and Grain Boundary Phases. *ACS Appl Mater Interfaces* **2020**, 12, 56118-56125.
- (48) Yi, E.; Wang, W.; Kieffer, J.; Laine, R. M. Flame Made Nanoparticles Permit Processing of Dense, Flexible, Li⁺ Conducting Ceramic Electrolyte Thin Films of Cubic-Li₇la₃zr₂o₁₂ (C-Llzo). *J. Mater. Chem. A* **2016**, 4, 12947-12954.
- (49) Xie, R.-C.; Shang, J. K. Morphological Control in Solvothermal Synthesis of Titanium Oxide. *J. Mater. Sci.* **2007**, 42, 6583-6589.
- (50) Dunne, P. W.; Munn, A. S.; Starkey, C. L.; Huddle, T. A.; Lester, E. H. Continuous-Flow Hydrothermal Synthesis for the Production of Inorganic Nanomaterials. *Philos. Trans. A Math. Phys. Eng. Sci.* **2015**, 373, 1-21.
- (51) Kobayashi, M.; Kato, H.; Kakihana, M. Synthesis of Titanium Dioxide Nanocrystals with Controlled Crystal-and Micro-Structures from Titanium Complexes. *SAGE* **2013**, 3, 1-10.
- (52) Xu, G.; Tao, Z.; Zhao, Y.; Zhang, Y.; Ren, Z.; Shen, G.; Han, G.; Wei, X. Solvothermal Synthesis, Characterization and Formation Mechanism of Single-Crystalline Srtio₃ Dense Spheres with Monoethanolamine as Reaction Medium Solvent. *CrystEngComm* **2013**, 15, 1439-1444.
- (53) Hu, L.; Wang, C.; Kennedy, R. M.; Marks, L. D.; Poeppelmeier, K. R. The Role of Oleic Acid: From Synthesis to Assembly of Perovskite Nanocuboid Two-Dimensional Arrays. *Inorg. Chem.* **2015**, 54, 740-745.
- (54) Hu, L.; Wang, C.; Lee, S.; Winans, R. E.; Marks, L. D.; Poeppelmeier, K. R. Srtio₃ Nanocuboids from a Lamellar Microemulsion. *Chem. Mater.* **2013**, 25, 378-384.

- (55) Chouiekh, A.; Naji, M.; Rjeb, A.; Ababou, Y.; Sayouri, S. Sol-Gel Synthesis and Structural Study of a Lithium Titanate Phase Li_{3x}la_{2/3-X}tio₃ as Solid Electrolyte. *IOP Conf. Series: Mater. Sci. Engineering* **2021**, 1160, 1-9.
- (56) Liu, S.; Huang, L.; Li, W.; Liu, X.; Jing, S.; Li, J.; O'Brien, S. Green and Scalable Production of Colloidal Perovskite Nanocrystals and Transparent Sols by a Controlled Self-Collection Process. *Nano.* **2015**, 7, 11766-11776.
- (57) Lin, X.; Wang, H.; Du, H.; Xiong, X.; Qu, B.; Guo, Z.; Chu, D. Growth of Lithium Lanthanum Titanate Nanosheets and Their Application in Lithium-Ion Batteries. *ACS Appl. Mater. Interfaces* **2016**, 8, 1486-1492.
- (58) Sugita, M., Tsuji, M., Abe, M. Synthetic Inorganic Ion-Exchange Materials. Lviii. Hydrothermal Synthesis of a New Layered Lithium Titanate and Its Alkali Ion Exchange. *Bull. Chem. Soc.* **1990**, 63, 1978-1984.
- (59) Zheng, N.; Li, X.; Yan, S.; Wang, Q.; Qiao, R.; Hu, J.; Fan, J.; Cao, G.; Shao, G. Nano-Porous Hollow Li_{0.5}la_{0.5}tio₃ Spheres and Electronic Structure Modulation for Ultra-Fast H₂s Detection. *J. Mater. Chem. A* **2020**, 8, 2376-2386.
- (60) Bertrand, C. E.; Sengers, J. V.; Anisimov, M. A. Critical Behavior of the Dielectric Constant in Asymmetric Fluids. *J. Phys. Chem. B* **2011**, 115, 14000-14007.
- (61) Yang, T.; Gordon, Z. D.; Chan, C. K. Synthesis of Hyperbranched Perovskite Nanostructures. *Cryst. Growth Des.* **2013**, 13, 3901-3907.
- (62) Kimijima, T.; Kanie, K.; Nakaya, M.; Muramatsu, A. Solvothermal Synthesis of Shape-Controlled Perovskite Mtio₃ (M = Ba, Sr, and Ca) Particles in H₂o/Polyols Mixed Solutions. *Mater. Trans.* **2014**, 55, 147-153.
- (63) Toby, B. H.; Von Dreele, R. B. Gsas-Ii: The Genesis of a Modern Open-Source All Purpose Crystallography Software Package. *J. Appl. Crystallogr.* **2013**, 46, 544-549.
- (64) Mousavi-Kamazani, M.; Alizadeh, S.; Ansari, F.; Salavati-Niasari, M. A Controllable Hydrothermal Method to Prepare La(Oh)₃ Nanorods Using New Precursors. *J. Rare Earths* **2015**, 33, 425-431.
- (65) Ma, X.; Zhang, H.; Ji, Y.; Xu, J.; Yang, D. Synthesis of Ultrafine Lanthanum Hydroxide Nanorods by a Simple Hydrothermal Process. *Mater. Lett.* **2004**, 58, 1180-1182.
- (66) Yamamoto, H.; Tahara, T.; Sugahara, Y.; Kuroda, K.; Kato, C. Synthesis of $La_{1-X}m_xtio_3$ (M = Na, K; $0 \le X \le 0.4$) and the Electrical Properties. *Phase Transit.* **1993**, 41, 137-141.
- (67) Bucheli, W.; Duran, T.; Jimenez, R.; Sanz, J.; Varez, A. On the Influence of the Vacancy Distribution on the Structure and Ionic Conductivity of a-Site-Deficient Li_xsr_xla_{2/3-X}tio3 Perovskites. *Inorg. Chem.* **2012**, 51, 5831-5838.
- (68) Lu, D.-L.; Zhao, R.-R.; Wu, J.-L.; Ma, J.-M.; Huang, M.-L.; Yao, Y.-B.; Tao, T.; Liang, B.; Zhai, J.-W.; Lu, S.-G. Investigations on the Properties of $\text{Li}_{3x}\text{la}_{2/3-x}\text{tio}_3$ Based All-Solid-State Supercapacitor: Relationships between the Capacitance, Ionic Conductivity, and Temperature. *J. Eur. Cer. Soc.* **2020**, 40, 2396-2403.
- (69) Borstnar, P.; Zuntar, J.; Spreitzer, M.; Drazic, G.; Daneu, N. Exaggerated Grain Growth and the Development of Coarse-Grained Microstructures in Lithium Lanthanum Titanate Perovskite Ceramics *J. Euro. Cer. Soc.* **2023**, 43, 1017-1027.
- (70) Bhalla, A. S.; Guo, R.; Roy, R. The Perovskite Structure—a Review of Its Role in Ceramic Science and Technology. *Mater. Res. Innov.* **2000**, 4, 3-26.
- (71) Duncan, F. M.; Kirk, C. A.; Skakle, J. M. S. *Isis Experimental Report, Technical Report; Rb No 9708*; Rutherford Appleton Lab., Oxfordshire, U.K., 1998.

- (72) Swamy, D. T.; Babu, K. E.; Veeraiah, V. Evidence for High Ionic Conductivity in Lithium–Lanthanum Titanate, Li₀₋₂₉la₀₋₅₇tio₃. *Bull. Mater. Sci.* **2013**, 36, 1115-1119.
- (73) Hu, M.; Pang, X.; Zhou, Z. Recent Progress in High-Voltage Lithium Ion Batteries. *J. Power Sources* **2013**, 237, 229-242.
- (74) Zhang, M., Jin, Z., Zhang, J., Guo, X., Yang, J., Li, W., Wang, X., Zhang, Z. Effect of Annealing Temperature on Morphology, Structure and Photocatalytic Behavior of Nanotubed H₂ti₂o₄(Oh)₂. *J. Mol. Cat. A: Chem.* **2004**, 217, 203-210.
- (75) Nateq, M. H.; Ceccato, R. Sol-Gel Synthesis of Tio₂ Nanocrystalline Particles with Enhanced Surface Area through the Reverse Micelle Approach. *Adv. Mater. Sci. Eng.* **2019**, 2019, 1-14.
- (76) Orellano, M. S.; Longo, G. S.; Porporatto, C.; Correa, N. M.; Falcone, R. D. Role of Micellar Interface in the Synthesis of Chitosan Nanoparticles Formulated by Reverse Micellar Method. *Coll. Surf. A: Physicochem. Eng. Asp.* **2020**, 599, 1-12.
- (77) Gorbunova, O. V.; Baklanova, O. N.; Gulyaeva, T. I.; Trenikhin, M. V.; Drozdov, V. A. Poly(Ethylene Glycol) as Structure Directing Agent in Sol–Gel Synthesis of Amorphous Silica. *Micropor. Mesopor. Mater.* **2014**, 190, 146-151.
- (78) Shi, Y.-C.; Feng, J.-J.; Lin, X.-X.; Zhang, L.; Yuan, J.; Zhang, Q.-L.; Wang, A.-J. One-Step Hydrothermal Synthesis of Three-Dimensional Nitrogen-Doped Reduced Graphene Oxide Hydrogels Anchored Ptpd Alloyed Nanoparticles for Ethylene Glycol Oxidation and Hydrogen Evolution Reactions. *Electrochim. Acta.* **2019**, 293, 504-513.
- (79) Wojnarowicz, J.; Opalinska, A.; Chudoba, T.; Gierlotka, S.; Mukhovskyi, R.; Pietrzykowska, E.; Sobczak, K.; Lojkowski, W. Effect of Water Content in Ethylene Glycol Solvent on the Size of Zno Nanoparticles Prepared Using Microwave Solvothermal Synthesis. *J. Nanomater.* **2016**, 2016, 1-15.
- (80) Sun, Y.; Wang, C.; Huang, W.; Zhao, G.; Duan, L.; Liu, Q.; Wang, S.; Fraser, A.; Guo, H.; Sun, X. One-Step Calcination Synthesis of Bulk-Doped Surface-Modified Ni-Rich Cathodes with Superlattice for Long-Cycling Li-Ion Batteries. *Angew Chem Int Ed Engl* **2023**, 62, e202300962.
- (81) Mukai, K.; Yashima, M.; Hibino, K.; Terai, T. Experimental Visualization of Interstitialcy Diffusion of Li Ion in B-Li₂tio₃. *ACS Appl. Energy Mater.* **2019**, 2, 5481-5489.
- (82) Hai, C.; Li, S.; Zhou, Y.; Zeng, J.; Ren, X.; Li, X. Roles of Ethylene Glycol Solvent and Polymers in Preparing Uniformly Distributed Mgo Nanoparticles. *J. Asian Cer. Soc.* **2018**, 5, 176-182.
- (83) Bohnke, O.; Emery, J.; Veron, A.; Fourquet, J. L.; Buzare, J. Y.; Florian, P.; Massiot, D. A Distribution of Activation Energies for the Local and Long-Range Ionic Motion Is Consistent with the Disordered Structure of the Perovskite Li_{3x}la_{2/3-x}tio₃. *Sol. State Ionics* **1998**, 109, 25-34.
- (84) Boulant, A.; Maury, P.; Emery, J.; Buzare, J. Y.; Bohnke, O. Efficient Ion Exchange of H⁺for Li⁺ in (Li_{0.30}la_{0.57}0_{0.13})Tio₃ Perovskite in Water: Protons as a Probe for Li Location. *Chem. Mater.* **2009**, 21, 2209-2217.
- (85) Boulant, A.; Emery, J.; Jouanneaux, A.; Buzaré, J.-Y.; Bardeau, J.-F. From Micro- to Nanostructured Fast Ionic Conductor Li_{0.30}la_{0.56}□_{0.13}tio₃: Size Effects on Nmr Properties. *J. Phys. Chem. C* **2011**, 115, 15575-15585.
- (86) Emery, J.; Buzare, J. Y.; Bohnke, O.; Fourquet, J. L. Lithium-7 Nmr and Ionic Conductivity Studies of Lanthanum Lithium Titanate Electrolytes. *Sol. State Ionics* **1997**, 99, 41-51.
- (87) Bohnke, O. Anomalies in Li⁺ Ion Dynamics Observed by Impedance Spectroscopy and ⁷li Nmr in the Perovskite Fast Ion Conductor (Li_{3x}la_{2/3-X} \square _{1/3-2x})Tio₃. *Sol. State Ionics* **2003**, 158, 119-132.